Japanese Journal of Applied Physics

The Japan Society of Applied Physics

ACCEPTED MANUSCRIPT

Tunneling magnetoresistance effect with controlled spin polarization based on Mn_3ZnN

To cite this article before publication: Qianqian Sun *et al* 2024 *Jpn. J. Appl. Phys.* in press https://doi.org/10.35848/1347-4065/ad42ea

Tunneling magnetoresistance effect with controlled spin polarization based on Mn_3ZnN

Qianqian Sun[1,2], Kang An[1,2]*, Leimei Sheng[1,2], and Xinluo Zhao[1,2]

[1]*Department of Physics, Shanghai University, Shanghai 200444, China.*

[2]*Institute of Low-dimensional Carbon and Device Physics, Shanghai University, Shanghai 200444, China*

E-mail: ankang@shu.edu.cn

Due to groundbreaking advantages, antiferromagnetic offers superior prospects for the next-generation memory devices. However, detecting their Néel vector poses great challenges. Mn_3ZnN, an antiperovskite antiferromagnetic, breaks $TP\tau$ and $U\tau$ symmetries, exhibiting $\boldsymbol{k}$-resolved spin polarization at Fermi surface. It's ideal for electrodes to generate tunneling magnetoresistance (TMR) effects, which hinges on electrode-barrier compatibility. Testing various insulators, we obtained 2000% TMR effects in $Mn_3ZnN/SrTiO_3/Mn_3ZnN$. Additionally, applying 2% biaxial stress increased the spin polarization to 35.24% in Mn_3ZnN, hinting at higher TMR potential. These findings provide valuable insights for experimental and industrial developments in the field of spintronics.

Antiferromagnetic (AFM) is gradually replacing ferromagnetic (FM) as the ideal material for the storage cells in the next-generation memory devices due to their near-zero net magnetization and rapid spin dynamics[1),2)], which enables spintronic devices a larger storage density and faster in reading and writing speed. TMR effect, known as one of the methods to detect the Néel vector i.e., the magnetic moment configuration, has a great deal of advantages such as a much larger electric signal when compared to the method of anisotropic magnetoresistance[3),4)] and a smaller device footprint as through spin-Hall effect[5),6)].

Historically, the TMR effect was produced in ferromagnetic tunnel junctions, in which insulator barriers were sandwiched by two FM materials[7)-10)] and the magnitude of TMR effect was calculated in practical as: $TMR = \left(\frac{G_P}{G_{AP}} - 1\right) \times 100\%$[11)]. Notably, numerous FMTJs, like CoFe/AlO_x/CoFe[7)] and CoFeB/MgO/CoFeB[12)], exhibit excellent TMR ratios of hundreds percents.

However, due to spin degenerate, detecting the magnetic configuration through TMR effect has been challenged in conventional AFM like MnPt and CuMnAs[13)-15)]. Recent breakthroughs are transforming this landscape. AFMs have been reported with can induce spin-splitting band structure even without spin-orbit coupling when breaking specific symmetry operations ($TP\tau$ and $U\tau$ symmetries)[15),16)], where T represents time reversal operation, P is space inversion operation, U stands for spinor symmetry and τ is lattice translation. There are bunches of AFM exhibit $\boldsymbol{k}$-dependent spin-splitting in moment space. Recently, Dong *et.al.* have predicted that antiferromagnetic tunnel junctions (AFMTJs) based on spin-splitting Mn_3Sn, exhibit 100% TMR effects using HfO_2 as potential barriers[17)]. Remarkably, the TMR effect has been verified in experimental of 100% at room temperature in MnPt/Mn_3Pt/MgO/Mn_3Pt AFMTJ[18)]. Meanwhile, AFMTJs with the structure of RuO_2/Barrier/RuO_2 has been reported of 100% TMR effect[19),20)]. Gautam Gurung *et.al*. predicted huge TMR effects in AFMTJs based on Mn_3GaN[21)], implied that TMR effect using AFM as electrodes has a lot of prospects yet to be discovered.

The recent research realized that, in noncollinear AFM, TMR effects stem from the mismatch of the spin texture between the electrodes since spin is no longer a good quantum number. Considering the impact of insulator barriers, TMR effects can reach up to a huge magnitude or reduce to almost none[18)], which depends on the lowest decay rates of the potential barriers in

2D Brillouin zone.

In this article, we focus on the antiperovskite antiferromagnet Mn_3ZnN. This material, characterized by the magnetic ground state of Γ_{5g}[22),23)], boasts a host of remarkable properties, including anomalous Hall effect[24)-26)], strong magnetocrystalline anisotropy[27)], magneto-optical effect[24)] and anomalous Nernst effect[28)], all of which have been reported recent years. Due to its spin-polarized band at the Fermi energy, we constructed the AFMTJs based on Mn_3ZnN electrodes to analyze the TMR effects compared with various insulator barriers. After we selected $SrTiO_3$, one of the most common materials in experiment, as barriers to calculate the TMR effects, we concluded that huge TMR effects results from the suitable of electrodes and barriers. Furthermore, we tested the spin polarization of the Mn_3ZnN under different biaxial stresses and obtained a maximum spin polarization of 35.24% at 2% stretching.

As illustrated in Fig. 1(a), noncollinear antiferromagnetic Mn_3ZnN, whose lattice constant is 3.902 Å[29)], belongs to antiperovskite structure. The magnetic space group (MSG) of Mn_3ZnN is R-3m, with the corresponding atoms position shown in TABLE SI in the Supplementary materials. The yellow and green vectors in Fig. 1(b) and 1(c) indicate the magnetic configurations of the two energy-equivalent ground states (positive and negative states) of Mn_3ZnN, in which the magnetic moments are within the (111) lattice plane with the adjacent Mn atom spin moment of 120 degrees angle. As mentioned earlier, the TMR effect of AFMTJs relies on the spin polarization of the antiferromagnetic electrodes, especially at the Fermi energy. Here, as shown in Fig. 1(e) and 1(f), through first principles calculations, we demonstrate the spin expectation value $<\boldsymbol{\sigma_x}>$, $<\boldsymbol{\sigma_y}>$ and $<\boldsymbol{\sigma_z}>$ projected band structure of bulk Mn_3ZnN, in which spins are polarized in the Brillouin zone along some high symmetric paths[30)]. The details of the calculations can refer to the Note 2 in the Supplementary materials. Moreover, the magnitude of the spin-splitting is significantly different in various paths according to some symmetry operation, e.g., huge along Γ-X-M, while hardly at all along M-Γ referring to the $<\boldsymbol{\sigma_z}>$ projected band structure of Mn_3ZnN, demonstrated in the right panel of the Fig. 1(e) and 1(f). The invisible spin-polarization of the $<\boldsymbol{\sigma_z}>$ along M-Γ is induced by the mirror plane shown in the Fig. 1(a), in which the $\boldsymbol{M_Z M_{[110]}}$ and $\boldsymbol{M_Z M_{[-110]}}$ operates as follows:

$$\boldsymbol{M_Z M_{[110]}(k_x, k_y, k_z\,;\, \sigma_x, \sigma_y, \sigma_z) = (-k_y, -k_x, -k_z\,;\, -\sigma_y, -\sigma_x, -\sigma_z)}$$

$$\boldsymbol{M_Z M_{[-110]}}(\boldsymbol{k_x}, \boldsymbol{k_y}, \boldsymbol{k_z}\ ;\ \boldsymbol{\sigma_x}, \boldsymbol{\sigma_y}, \boldsymbol{\sigma_z}) = (\boldsymbol{k_y}, \boldsymbol{k_x}, -\boldsymbol{k_z}\ ;\ -\boldsymbol{\sigma_y}, -\boldsymbol{\sigma_x}, -\boldsymbol{\sigma_z})$$

Where $\boldsymbol{k_x}$, $\boldsymbol{k_y}$ and $\boldsymbol{k_z}$ are the coordinates in the Brillouin zone, while $\boldsymbol{\sigma_x}$, $\boldsymbol{\sigma_y}$ and $\boldsymbol{\sigma_z}$ represent the component of spin expectation value in Cartesian coordinates. The mirror symmetric operation restricts the band structures along the M-Γ line to be spin-degenerate. In addition, all of the spin expectation values have reversed when flipping the magnetic moment at the corresponding $\boldsymbol{k}$-points, enhancing TMR effects when utilized as electrodes in AFMTJs.

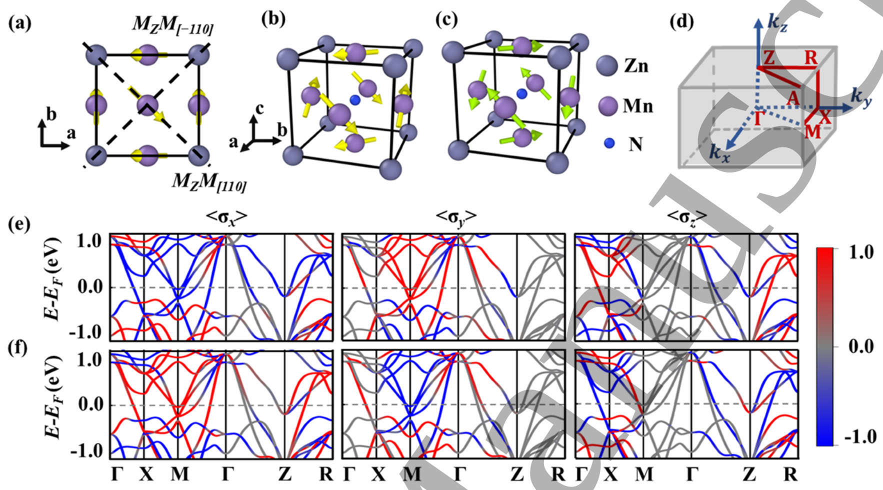

Fig. 1(a) Mirror operations representation on the top view of the bulk Mn_3ZnN. (b-c) Atomic structure of noncollinear antiferromagnetic Mn_3ZnN under positive and negative magnetic configuration. (d) High symmetric line in the Brillouin zone of the Tetragonal phase. (e-f) Band structure with projected spin expectation value $<\sigma_x>$, $<\sigma_y>$ and $<\sigma_z>$ (from left to right) of Mn_3ZnN under positive and negative magnetic configuration.

Apart from the spin-polarized electrodes, the TMR effect is strongly influenced by the potential barrier. Sometimes an improper insulator can result in an almost negligible TMR effect, which primarily due to inevitable interface roughness arising from lattice constant incoherence between electrodes and barriers, or a mismatch between the lowest decay rates of evanescent states in barriers and spin-polarization in electrodes within the 2D Brillouin zone[18)], which severely hampers the application of AFMTJs.

To access the impact of various potential barrier on transmission, we employed the factorized transmission function $T(\boldsymbol{k}_{\parallel})$, which has the format as follows[31),32)]:

$$T_\sigma(\boldsymbol{k}_\parallel) = t_L^\sigma(\boldsymbol{k}_\parallel)\exp[-2\kappa(\boldsymbol{k}_\parallel)d]\, t_R^\sigma(\boldsymbol{k}_\parallel), \quad (1)$$

Where κ is the smallest decay rates of the evanescent states, d stands for the thickness (in the units of Å) of the potential barriers, $t_L^{\sigma}(\boldsymbol{k}_{\parallel})$ and $t_R^{\sigma}(\boldsymbol{k}_{\parallel})$ represent the surface transmission function of the left and right electrodes, respectively. As illustrated in Fig. 2(a), when electrons are transported from left to right lead and encounter the two interfaces, they will be tunneled as follows[32)]:

$$t_L^{\sigma}(\boldsymbol{k}_{\parallel}) = \sum_{in} \left|\frac{L_{out}}{L_{in}}\right|^2, \qquad t_R^{\sigma}(\boldsymbol{k}_{\parallel}) = \sum_{out} \left|\frac{R_{out}}{R_{in}}\right|^2, \tag{2}$$

Where L_{out}, L_{in}, R_{out} and R_{in} are the amplitudes of the tunneling eigenstates according to the incident and outgoing waves at the left and right interfaces.

In order to prevent the considerable interface roughness, dislocations and other defects caused by the large lattice mismatch of the electrodes and barriers during the growth in experimental, we have screened some insulators with ab-axis lattice constant close to those of Mn_3ZnN from Crystallography Open Database[33),34)]. As demonstrated in Fig. 2(b), all suitable insulating materials were categorized into five sections, and the TMR ratio in the AFMTJs based on Mn_3ZnN electrodes was estimated using equation (1). For clarity, all of the TMR ratio were normalized with the value derived using $SrTiO_3$, one of the most common materials in experiments, as potential barriers. Among these materials, relatively high TMR effects were observed with barriers such as SrHCl, NaCuSe, ZnK_2F_2, $SrTiO_3$, and $CaZrO_3$ *etc.*, suggesting their suitability with Mn_3ZnN.

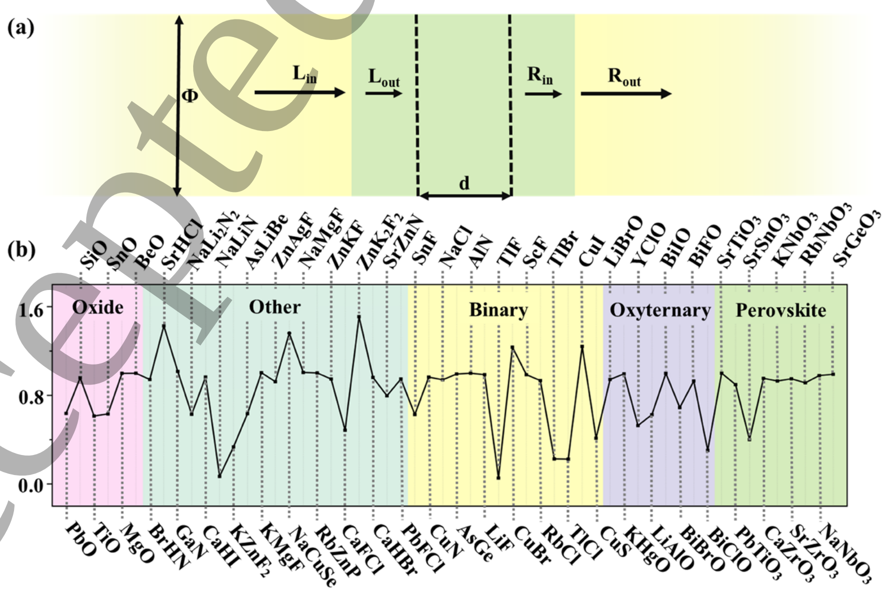

Fig. 2(a) Schematic diagram of the tunnel junction, in which the yellow parts represent the electrodes, while the green part stand for the area of potential barrier with the thickness of *d* Å. (b) TMR effects using various insulator barriers under the normalization of TMR ratio estimated in $Mn_3ZnN/SrTiO_3/Mn_3ZnN$.

In order to learn more about the essence of the large TMR effects, we selected one of the suitable materials, $SrTiO_3$ as a representative material for analysis. Although some insulators mentioned in Fig. 2(b) have the ability to exhibit huger TMR effect, experimentally perovskite grows more maturely on Mn_3ZnN, the antiperovskite substrates.

Subsequently, we constructed the AFMTJs based on Mn_3ZnN electrodes with $SrTiO_3$ as insulating barriers. As illustrated in Fig. 3(a), the schematic of the $Mn_3ZnN/SrTiO_3/Mn_3ZnN$ structure is the result of energy competition at the interface, which demonstrated in Fig. S1(b) of Supplementary materials. We determined the most energy-stable interface distance to be 2.1 Å.

Employing first principles calculation with linear ballistic conductance[35),36)], we calculated the TMR ratio of AFMTJs based on Mn_3ZnN with $SrTiO_3$ as insulator barriers in parallel and antiparallel configurations. The calculated G_P/G_{AP} in $Mn_3ZnN/SrTiO_3/Mn_3ZnN$ can reach up to 20.64, corresponding to a conventional TMR ratio of 2000%, significantly larger than previously predicted TMR effects[17),18)]. The tunneling conductance in a unit area can be transformed by the ***k***-dependent transmission like this[21)]:

$$G = \frac{e^2}{h}\frac{1}{(2\pi)^2}\int T(\boldsymbol{k}_\parallel)d\boldsymbol{k}_\parallel, \tag{3}$$

Where $T(\boldsymbol{k}_\parallel)$ is the ***k***-dependent transmission in AFMTJs. As depicted in Fig. 3(e) and 3(f), the transmission within the 2D Brillouin zone distribution significantly decreases when the magnetic configuration switches to antiparallel, particularly for certain ***k***-points near half the distance from edge to the Γ-point. This phenomenon arises due to the combined effects of ***p*** from Mn_3ZnN and κ from $SrTiO_3$ within the 2D Brillouin zone.

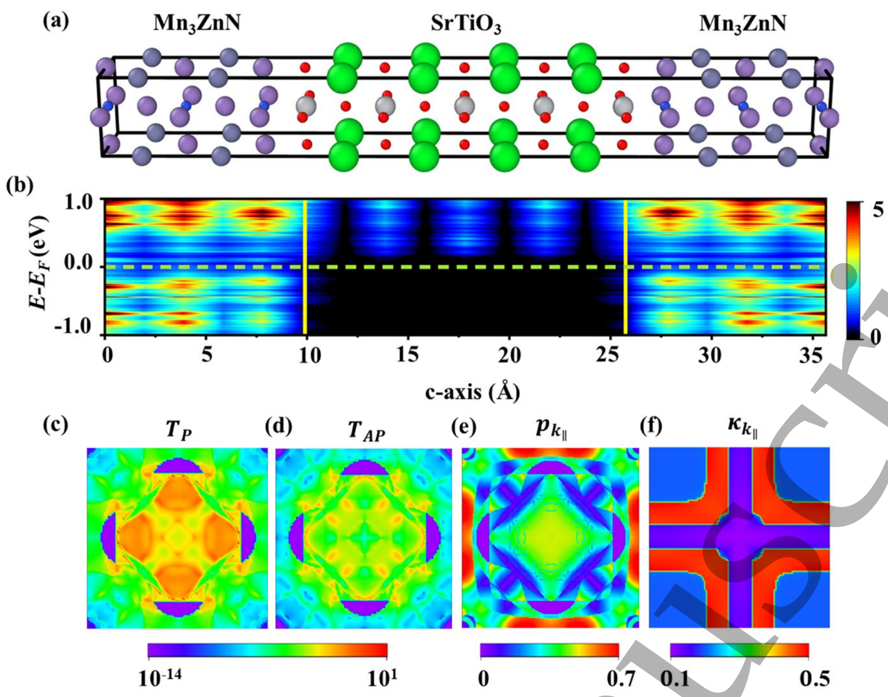

Fig. 3(a) Schematic of the AFMTJs based on Mn_3ZnN with $SrTiO_3$ as potential barriers, in which the same magnetic configuration of the two leads for parallel configuration, while opposite for antiparallel states. (b) LDOS of the AFMTJs corresponding to (a), the vertical yellow line divided the x axis into left lead, insulator barrier and right lead area, respectively. The green dash line represents the Fermi energy. (c-d) Transmission of the $Mn_3ZnN/SrTiO_3/Mn_3ZnN$ for parallel and antiparallel state. (e) $\boldsymbol{k}$-dependent spin polarization distribution of bulk Mn_3ZnN. (f) $\boldsymbol{k}$-dependent lowest decay rates of insulator $SrTiO_3$ in 2D Brillouin zone.

As for the spin polarization, in collinear materials, the tot spin channels are summed as $s_{tot} = s_N^{\uparrow} + s_N^{\downarrow}$ since the spin operator is a good quantum number. Here, $s_N^{\uparrow}$ and $s_N^{\downarrow}$ represent the spin channels for up (↑) and down (↓) spins, respectively. As the representation of the magnitude of spin-splitting, spin polarization, in collinear system, has the following definition:

$$\boldsymbol{p}_{\boldsymbol{k}_\parallel} = \frac{s_N^{\uparrow}(\boldsymbol{k}_\parallel) - s_N^{\downarrow}(\boldsymbol{k}_\parallel)}{s_N^{\uparrow}(\boldsymbol{k}_\parallel) + s_N^{\downarrow}(\boldsymbol{k}_\parallel)}, \tag{4}$$

Where $\boldsymbol{p}$ denotes the spin polarization, and $\boldsymbol{k}_\parallel$ represents k-resolved in the Brillouin zone. The net spin polarization in the entire Brillouin zone is a sum of $\boldsymbol{p}_{\boldsymbol{k}_\parallel}$, i.e., $\boldsymbol{p} = \sum_{\boldsymbol{k}_\parallel} \boldsymbol{p}_{\boldsymbol{k}_\parallel}\, \omega_{\boldsymbol{k}_\parallel}$. Where $\omega_{\boldsymbol{k}_{||}}$ represents the weight of corresponding $\boldsymbol{k}$-points in the Brillouin zone.

However, in noncollinear systems, the spin operator is no longer a good quantum number and has the format of vector including $\mathbf{s_x}$, $\mathbf{s_y}$ and $\mathbf{s_z}$. Therefore, spin polarization at a single $\boldsymbol{k}$-point is defined as:

$$\boldsymbol{p}_{\boldsymbol{k}_\parallel} = \frac{\boldsymbol{s}(\boldsymbol{k}_\parallel)}{|\boldsymbol{s}_n|}, \tag{5}$$

Here, s_n is the normalized spin vector, and the net spin polarization in the entire Brillouin zone also formulates: $\boldsymbol{p} = \sum_{\boldsymbol{k}_\parallel} \boldsymbol{p}_{\boldsymbol{k}_\parallel} \omega_{\boldsymbol{k}_\parallel}$. As demonstrated in Fig. 3(e), utilizing first principles calculations, we observed a considerable spin polarization of 32.08% in cubic Mn_3ZnN, the distribution of which shows a significant spin polarization near the four edges and in a large area around Γ-center.

In terms of the κ in barrier materials, Fig. 3(f) illustrate the distribution of the lowest decay rates of the evanescent states, i.e., the smallest imaginary part of complex band κ in the 2D Brillouin zone of $SrTiO_3$. Notably, a cross-shaped pattern of lower decay rates is observed near the Γ-point and likewise in a large area of the four corners. The combination of the κ of $SrTiO_3$ and the $\boldsymbol{p}$ of Mn_3ZnN contribute to considerable TMR effects, as mentioned of 2000%. The distribution of κ for all insulators mentioned in Fig. 2(b) has been detailed in Fig. S2 of the Supplementary materials in which κ influences the transmission via the term $\exp[-2\kappa(\boldsymbol{k}_\parallel)d]$ in formula (1), and the barrier's thickness directly correlates with transmission. Meanwhile, as depicted in Fig. 3(b), we computed the layer-resolved density of states (LDOS), which indicates that the Fermi energy of the tunnel junction falls within the bandgap of the insulator barrier $SrTiO_3$.

To access the impact of d in equation (1), we investigated the effects of reducing the thickness of the $SrTiO_3$ layer in AFMTJs based on Mn_3ZnN, which resulted in a reduction of the TMR ratio from 2000% to approximately 1300%, corresponding to a decrease in $SrTiO_3$ thickness from 1.6 to 0.8 nm. Thinner barriers in the AFMTJs provide insights into the intrinsic transport abilities of the electrodes themselves, and the lower TMR effect value reiterates that $SrTiO_3$ is a suitable insulator barrier when used with Mn_3ZnN in AFMTJs to facilitate electrical transport capacity throughout the Brillouin zone.

The transport abilities of Mn_3ZnN can be expressed by the spin polarization within the Brillouin zone. Thus, we investigated the $\boldsymbol{p}_{\boldsymbol{k}_\parallel}$ under the biaxial stress ranging from -5% to 5%

to show the impact of electrodes. As depicted in Fig. 4(a), the spin polarization across the Brillouin zone increases to 35.24% when the ab-axis is stretched to 2%, followed by a decrease upon further stretching, while remaining relatively insensitive to biaxial compression. The maps of the spin polarization in Fig. 4(b-c) reveal that at 2% biaxial stress, significant spin polarization is observed at crossroads as well as the center area, aligning remarkably well with the extremely low κ in the center region of $SrTiO_3$, which holds strong promise for producing giant TMR effects. Meanwhile, the reduction in the total spin polarization under 4% and 5% stretch is attributed to the large purple regions in Fig. 4(c), where none of the bands cross the Fermi energy.

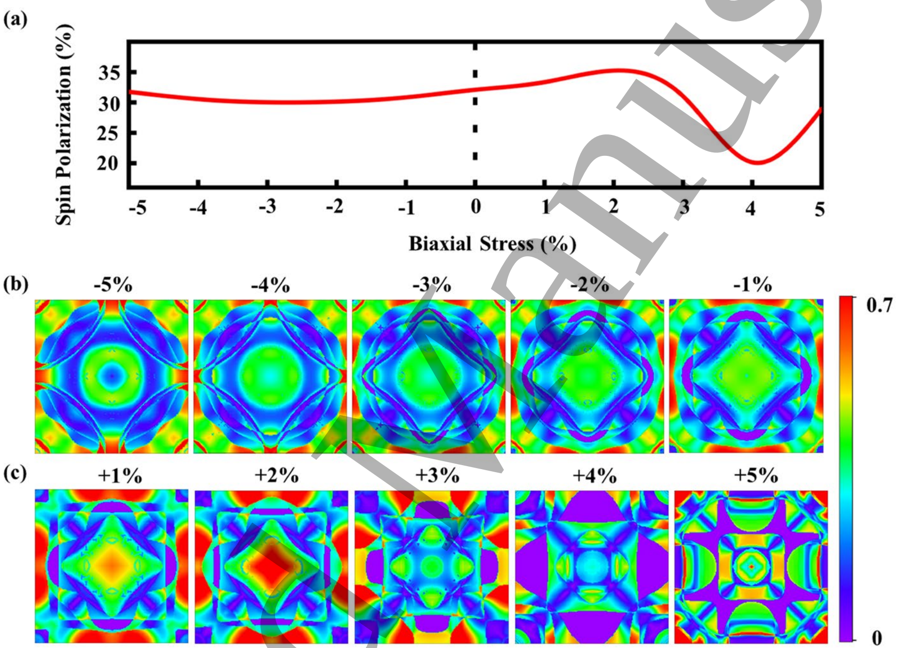

Fig. 4(a) Variation of spin polarization of the bulk Mn_3ZnN at the Fermi energy with biaxial stress from -5% to 5%. (b-c) Spin polarization distribution in the 2D Brillouin zone with the compression from -5% to -1% in (b) and stretch from 1% to 5% in (c).

Finally, we calculated the TMR effect in the AFMTJs based on Mn_3ZnN under a 2% biaxial stress, with shorter $SrTiO_3$ barrier of 0.8 nm mentioned above. This configuration exhibits a better response to the properties of electrodes. Notably, as demonstrated in Fig. S3 in Supplementary materials, upon integrating the transmission across the Brillouin zone, the TMR ratio experienced a tremendous boost, increasing by fivefold compared to AFMTJs based on original Mn_3ZnN, reaching 6000%. This result strongly validates the premise that a larger spin polarization contributes to a better TMR effect.

In summary, due to $TP\tau$ and $U\tau$ symmetries breaking, Mn_3ZnN, an antiperovskite AFM exhibits ***k***-resolved spin polarization suitable for use as electrodes in AFMTJs to detect Néel vector through TMR effects. Following extensive testing of insulators, we selected $SrTiO_3$ as barriers. Using density functional theory and linear ballistic conductance formula, we calculated a TMR ratio of up to 2000% in AFMTJs based on Mn_3ZnN. Furthermore, we estimated the spin polarization of bulk Mn_3ZnN under biaxial stress, finding that at 2% stretch, the spin polarization can reach up to 35.24%. Importantly, the distribution of spin polarization in 2D Brillouin zone closely matches the lowest decay rates of $SrTiO_3$, suggesting that AFMTJs based on 2% stretched Mn_3ZnN with $SrTiO_3$ may achieve even higher TMR effects. These findings and underlying principles offer valuable insights for the experimental and practical development of spintronics devices based on AFMTJs.

Acknowledgments

This work is supported by the National Natural Science Foundation of China (Grant Nos. 52071194).

References

1) T. Jungwirth, J. Sinova, A. Manchon, X. Marti, J. Wunderlich and C. Felser, Nat. Phys. **14**, 200 (2018).

2) V. Baltz, A. Manchon, M. Tsoi, T. Moriyama, T. Ono and Y. Tserkovnyak, Rev. Mod. Phys. **90**, 015005 (2018).

3) S.Y. Bodnar, L. Šmejkal, I. Turek, T. Jungwirth, O. Gomonay, J. Sinova, A.A. Sapozhnik, H.J. Elmers, M. Kläui and M. Jourdan, Nat. Commun. **9**, 348 (2018).

4) P. Wadley, B. Howells, J. Železny, C. Andrews, V. Hills, R.P. Campion, V. Novák, K. Olejník, F. Maccherozzi, S.S. Dhesi, S.Y. Martin, T. Wagner, J. Wunderlich, F. Freimuth, Y. Mokrousov, J. Kuneš, J.S. Chauhan, M.J. Grzybowski, A.W. Rushforth, K.W. Edmonds, B.L. Gallagher and T. Jungwirth, Science. **351**, 587 (2016).

5) G.R. Hoogeboom, A. Aqeel, T. Kuschel, T.T.M. Palstra and B.J. van Wees, Appl. Phys. Lett. **111**, 052409 (2017).

6) J. Fischer, O. Gomonay, R. Schlitz, K. Ganzhorn, N. Vlietstra, M. Althammer, H. Huebl, M. Opel, R. Gross, S.T.B. Goennenwein and S. Geprägs, Phys. Rev. B **97**, 014417 (2018).

7) J.S. Moodera, L.R. Kinder, T.M. Wong and R. Meservey, Phys. Rev. Lett. **74**, 3273 (1995).

8) S. Yuasa, T. Nagahama, A. Fukushima, Y. Suzuki and K. Ando, Nat. Mater. **3**, 868 (2004).

9) S.S. Parkin, C. Kaiser, A. Panchula, P.M. Rice, B. Hughes, M. Samant and S.H. Yang, Nat. Mater. **3**, 862 (2004).

10) R. Meservey and P.M. Tedrow, Phys. Rep. **238**, 173 (1994).

11) E.Y. Tsymbal, O.N. Mryasov and P.R. LeClair, J. Phys.-Condes. Matter **15**, R109 (2003).

12) D. D. Djayaprawira, K. Tsunekawa, M. Nagai, H. Maehara, S. Yamagata, N. Watanabe, S. Yuasa and K. Ando, Appl. Phys. Lett. **86**, 092502 (2005).

13) F. Máca, J. Kudrnovský, V. Drchal, K. Carva, P. Baláž and I. Turek, Phys. Rev. B. **96**, 094406 (2017).

14) P. Wadley, V. Hills, M.R. Shahedkhah, K.W. Edmonds, R.P. Campion, V. Novák, B. Ouladdiaf, D. Khalyavin, S. Langridge, V. Saidl, P. Nemec, A.W. Rushforth, B.L. Gallagher, S.S. Dhesi, F. Maccherozzi, J. Železny and T. Jungwirth, Sci. Rep. **5**, 17079 (2015).

15) L.-D. Yuan, Z. Wang, J.-W. Luo and A. Zunger, Phys. Rev. Mater. **5,** 014409 (2021).

16) S. Hayami, Y. Yanagi and H. Kusunose, J. Phys. Soc. Jpn. **88**, 123702 (2019).

17) J. Dong, X. Li, G. Gurung, M. Zhu, P. Zhang, F. Zheng, E.Y. Tsymbal and J. Zhang, Phys. Rev. Lett. **128**, 197201 (2022).

18) P. Qin, H. Yan, X. Wang, H. Chen, Z. Meng, J. Dong, M. Zhu, J. Cai, Z. Feng, X. Zhou, L. Liu, T. Zhang, Z. Zeng, J. Zhang, C. Jiang and Z. Liu, Nature **613**, 485 (2023).

19) L. Šmejkal, A.B. Hellenes, R. González-Hernández, J. Sinova and T. Jungwirth, Phys. Rev. X **12**, 011028 (2022).

20) D.F. Shao, S.H. Zhang, M. Li, C.B. Eom and E.Y. Tsymbal, Nat. Commun. **12**, 7061 (2021).

21) G. Gurung, K.-F. Shao and E.Y. Tsymbal, arXiv:2306.03026.

22) D. Fruchart and E. F. Bertaut, J. Phys. Soc. Jpn. **44**, 781 (1978).

23) S. Deng, Y. Sun, L. Wang, Z. Shi, H. Wu, Q. Huang, J. Yan, K. Shi, P. Hu, A. Zaoui and C. Wang, J. Phys. Chem. C **119**, 24983 (2015).

24) X. Zhou, J.-P. Hanke, W. Feng, F. Li, G.-Y. Guo, Y. Yao, S. Blügel and Y. Mokrousov, Phys. Rev. B **99**, 104428 (2019).

25) J.M.D. Coey, D. Givord and D. Fruchart, ECS J. Solid State Sci. Technol. **11**, 055002 (2022).

26) V.T.N. Huyen, M.-T. Suzuki, K. Yamauchi and T. Oguchi, Phys. Rev. B **100**, 094426 (2019).

27) H.K. Singh, I. Samathrakis, N.M. Fortunato, J. Zemen, C. Shen, O. Gutfleisch and H. Zhang, npj Comput. Mater. **7**, 98 (2021).

28) X. Zhou, J.-P. Hanke, W. Feng, S. Blügel, Y. Mokrousov and Y. Yao, Phys. Rev. Mater. **4**, 024408 (2020).

29) D. Fruchart, E.F. Bertaut, R. Madar and R. Fruchart, J. Phys. **32**, C1-876 (1971).

30) W. Setyawan and S. Curtarolo, Comput. Mater. Sci. **49**, 299 (2010).

31) J.P. Velev, C.G. Duan, J.D. Burton, A. Smogunov, M.K. Niranjan, E. Tosatti, S.S. Jaswal and E.Y. Tsymbal, Nano Lett. **9**, 427 (2009).

32) K.D. Belashchenko, E.Y. Tsymbal, M. van Schilfgaarde, D.A. Stewart, I.I. Oleynik and S.S. Jaswal, Phys. Rev. B **69**, 174408 (2004).

33) A. Vaitkus, A. Merkys, T. Sander, M. Quirós, P.A. Thiessen, E.E. Bolton and S. Gržulis, J. Cheminformatics **15**, 123 (2023).

34) A. Merkys, A. Vaitkus, A. Grybauskas, A. Konovalovas, M. Quirós and S. Gražulis, J. Cheminformatics **15**, 25 (2023).

35) S. Datta, Electronic transport in mesoscopic systems, (University Press, Cambridge, 1995) p.48.

36) M.D. Ventra, Electrical Transport in Nanoscale Systems, (University Press, Cambridge, 2008) p.39.